Available online at www.sciencedirect.com

SCIENCE DIRECT®

Journal of Solid State Chemistry 179 (2006) 1259–1272

JOURNAL OF SOLID STATE CHEMISTRY

www.elsevier.com/locate/jssc

The evolution of structural changes in ettringite during thermal decomposition

Michael R. Hartman[a,*], Steven K. Brady[b], Ronald Berliner[a], Mark S. Conradi[b]

[a] *University of Michigan, Ann Arbor, MI 48109, USA*
[b] *Department of Physics, Washington University, CB 1105, St. Louis, MO 63130, USA*

Received 7 September 2005; received in revised form 15 December 2005; accepted 15 January 2006
Available online 23 February 2006

Abstract

The thermal decomposition of ettringite, $Ca_6[Al(OH)_6]_2(SO_4)_3 \cdot {\sim}26H_2O$, was studied with pulsed neutron time-of-flight diffraction combined with Rietveld structure refinement. Like prior investigations, transition from a crystalline to amorphous state occurred following the loss of ~20 water molecules. In contrast to earlier investigations, which relied upon indirect measurements of water and hydroxyl occupancies, the present study inferred the occupancies directly from Rietveld crystal structure refinement of the diffraction data. The decomposition pathway was shown to be more complex than previously envisioned, involving the simultaneous loss of hydroxyl and water molecules. Nuclear magnetic resonance (NMR) spectroscopy studies of the rigid lattice lineshapes of fully and partially hydrated ettringite were performed and confirmed our decomposition model.
© 2006 Elsevier Inc. All rights reserved.

Keywords: Thermal treatment; Neutron powder diffraction; Spectroscopy; Physical properties; Calcium aluminate cement; Ettringite

1. Introduction

Ettringite, $Ca_6[Al(OH)_6]_2(SO_4)_3 \cdot {\sim}26H_2O$, is a rarely occurring mineral in nature, but it is prevalent in the chemistry of Portland cements. The initial setting rate of the highly reactive calcium aluminate phase, $Ca_3Al_2O_6$, in Portland cements is controlled by the addition of a setting retarder such as gypsum, $CaSO_4 \cdot 2H_2O$. Hydration of the calcium aluminate phase in the presence of gypsum leads to the formation of an ettringite membrane about the calcium aluminate grains, thus lowering the hydration rate [1]. Additionally, the growth of ettringite in mature cement pastes has been linked to the destructive mechanisms of sulfate attack [2] and delayed ettringite formation [3]. A recent investigation of the structure of ettringite, using pulsed neutron time-of-flight (TOF) diffraction techniques in combination with Rietveld crystal structure refinement, provided an improved understanding of the ettringite crystalline structure [4]. The thermal decomposition of ettringite has been studied in some detail by many prior investigations, yet many questions remain as to the exact nature of the structural changes that arise during the dehydration process. The present study utilizes pulsed neutron TOF diffraction techniques, Rietveld crystal structure refinement, and ^1H nuclear magnetic resonance (NMR) spectroscopy to gain an improved understanding of the thermal decomposition pathway of ettringite.

An early study of the thermal dehydration of ettringite by Bannister et al. [5] examined the changes in a natural specimen of ettringite using X-ray methods. They observed a decrease in the *a*-axis from 1.124 to 0.84 nm along with a marked decrease in the *c*-axis from 2.145 to 1.021 nm upon dehydrating a single crystal of ettringite at 110 °C. The near halving of the *c*-axis was attributed to an increase in symmetry concomitant with the dehydration process. Skoblinskaya and Krasilnikov [6,7] studied the dehydration isotherms of ettringite, using X-ray diffraction, crystal optical, and scanning electron microscopy (SEM) techniques, by varying the partial pressure of water vapor to which a synthetic ettringite sample was exposed. Based upon the structural work of Moore and Taylor [8] along

---

[*] Corresponding author. National Institute of Standards and Technology, 100 Bureau Drive, MS 8562, Gaithersburg, MD 20899-8562, USA. Fax: +1 301 921 9847.

E-mail address: michael.hartman@nist.gov (M.R. Hartman).

0022-4596/$ - see front matter © 2006 Elsevier Inc. All rights reserved.
doi:10.1016/j.jssc.2006.01.038

with the results of their own work, Skoblinskaya and Krasilnikov suggested that ettringite contained four distinct types of water and that the dehydration process followed an orderly, sequential removal of water from these sites. Shimada and Young [9] utilized thermogravimetric analysis (TGA) along with X-ray diffraction and ^{27}Al NMR spectroscopy to follow the thermal dehydration process. The results of Shimada and Young indicated that during the early stages of dehydration, the dehydration followed the sequential process proposed by Skoblinskaya and Krasilnikov, but that at later times the dehydration process was more complicated. The exact details of the dehydration process proposed by Skoblinskaya and Krasilnikov and the deviations from that process observed by Shimada and Young will be further discussed in conjunction with the results of the present work.

2. Experimental

2.1. Ettringite synthesis

Hydrogen is problematic for structural determinations using neutron scattering because it has a large incoherent cross-section that contributes to the background signal and leads to data with a poor signal-to-noise ratio. Therefore, the ettringite used in the neutron diffraction investigation was prepared with deuterium in place of hydrogen. Using a glove box with an inert nitrogen atmosphere, a solution of 0.07884 moles of deuterated calcium hydroxide, $Ca(OD)_2$, in 650 cc of D_2O was mixed with another solution of 0.01314 moles of anhydrous aluminum sulfate, $Al_2(SO_4)_3$, in 150 cc of D_2O. The combined mixture was magnetically stirred for a period of 24 h after which the precipitated ettringite was vacuum-filtered and allowed to dry over a saturated solution of LiCl in D_2O (11% RH). The dried ettringite was subjected to X-ray diffraction, TGA, and SEM analyses to characterize the material. Pulsed neutron TOF diffraction data were collected on the ettringite using the Special Environment Powder Diffractometer (SEPD) [10] at the Intense Pulsed Neutron Source (IPNS) of Argonne National Laboratory. The TOF neutron diffraction data were refined, using the Rietveld crystal structure refinement method, in the $P31c$ space group, and the lattice parameters at 10 K were determined to be $a = 1.166881(82)$ nm and $c = 2.135366(22)$ nm. Further details on the characterization and the results of the structural investigation, employing pulsed neutron TOF diffraction in conjunction with Rietveld crystal structure refinement, can be found in a recent article by Hartman and Berliner [4].

The NMR study measured signals from hydrogen nuclei, so regular ^{1}H ettringite was suitable. We synthesized the ettringite in a method analogous to the ^{2}D ettringite synthesis described above, but using H_2O and $Ca(OH)_2$ instead of D_2O and $Ca(OD)_2$. The dried ^{1}H ettringite was also subjected to X-ray diffraction, TGA, SEM, and ICP optical emission spectroscopy analyses to characterize the material.

In all of our work, handling of the samples was done in a glovebag under an inert atmosphere to preclude interaction with CO_2, rehydration, or D–H exchange as a result of contact with moist air.

2.2. Ettringite dehydration

The structural changes associated with the thermal decomposition of ettringite were investigated using pulsed neutron TOF diffraction techniques on the SEPD instrument at the IPNS in conjunction with Rietveld crystal structure refinement. Data from the $\pm 44°$, $\pm 90°$, and $\pm 145°$ SEPD detector banks were simultaneously utilized in performing a Rietveld crystal structure refinement [11] of the data for the ettringite samples. The Rietveld crystal structure refinement, denoted simply as structural refinement from this point forward, employed the *GSAS* [12] computer code as implemented in *EXPGUI* [13]. The structural refinement applies a non-linear least-squares fitting of a crystalline structural model to the diffraction data [14]. The structural model is modified and compared to the data in an iterative fashion until close agreement between the model and the data is achieved. The investigation used two different experimental methodologies. In the first, fully hydrated ettringite was loaded into a specially designed sample holder. The sample holder was equipped with heating blocks located at the top and bottom to maintain isothermal conditions throughout the sample. In addition, the sample holder was engineered to allow gas flow through a sintered metallic filter located at the bottom of the sample. A cross-sectional view of the sample holder is shown schematically in Fig. 1. Using this arrangement, the dehydration process was followed in situ by heating to the desired temperature and then initiating a controlled flow of dried nitrogen gas through the specimen holder. A plug of quartz wool was held in place at the top of the sample by a piece of perforated tape to prevent the loss of any of the specimen. In situ dehydration employed 1.258 g of ettringite. Initially the ettringite was loaded into the cell and data were collected at 40 °C with the tape at the top of the specimen holder not perforated and the nitrogen flow stopped to permit analysis of the sample in an unaltered state. These static data were collected at 40 °C to minimize the likelihood that the sample would be thermally affected prior to the actual dehydration study. Following the collection of data for approximately 21 h at 40 °C, the sample holder was removed from the SEPD instrument, the tape at the top perforated, and the heating blocks adjusted to maintain a stable temperature of 50 °C. The sample holder was then replaced into the SEPD instrument and a flow of dry nitrogen was initiated at 25 cc/min. The nitrogen was passed through a desiccant cartridge prior to entering the sample holder to remove any moisture from the gas. Data were collected in 1 h data sets for a period of 40 h as the sample dehydrated.

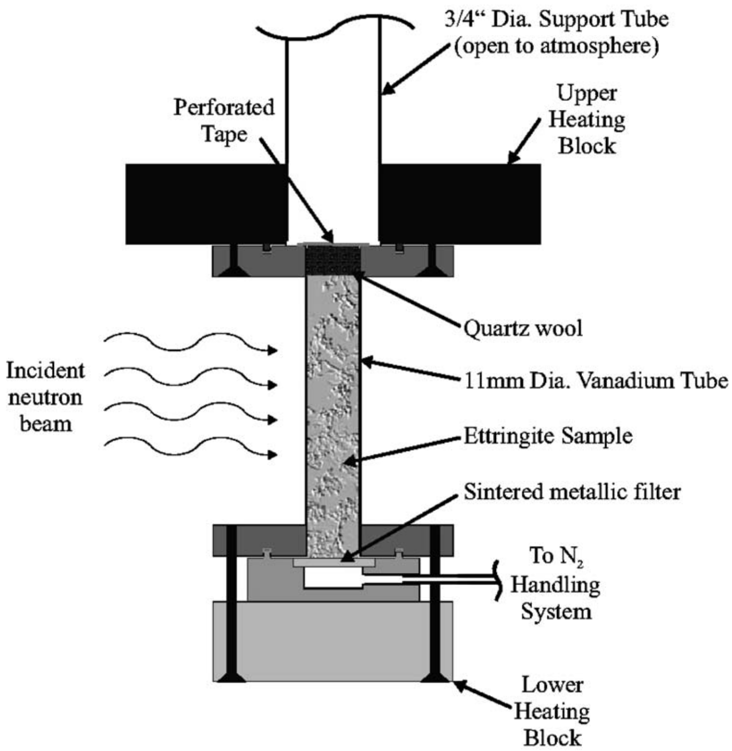

Fig. 1. A schematic illustration of the cross section of the in situ dehydration sample holder.

In the second neutron diffraction experimental methodology, ettringite was subjected to a heat treatment process in the laboratory to known weight losses of 6.16%, 15.6%, 20.5%, and 27.1%. The laboratory dehydration was conducted by placing a thin layer of ettringite in an air-tight container and then flowing dry nitrogen gas across the sample which was maintained at ~45 °C. The use of a thin layer of ettringite ensures that there is less chance for stratification compared to the in situ arrangement. The samples were periodically weighed until the desired weight loss was achieved. Pulsed neutron TOF diffraction data were collected on each sample, using the SEPD instrument at the IPNS, by placing it in a standard vanadium sample cell. Data collections were conducted at 10 K to minimize the thermal motions of the atoms and allow for a precise determination of their equilibrium positions.

Laboratory dehydration of the ^{1}H ettringite samples for NMR study to measured weight losses of 6.98% and 19.9% was done in an analogous manner to the latter method described above. Proton NMR spectra were obtained at 39.99 and 85.04 MHz, and at various temperatures from 296 K down to 77 K. The rigid-lattice NMR spectra (the limiting low-temperature spectra) were then compared with theoretical lineshapes based on atomic positions from our Rietveld crystal structure refinements, and hydrogen site occupancies given by our model of dehydration and that of Shimada and Young [9]. Especially at the 19.9% weight loss level, the two models of dehydration were well differentiated in their theoretical predictions.

3. Discussion

3.1. Ettringite composition and structure

The results of the previous pulsed neutron TOF investigation into the structure of ettringite [4] indicate that the chemical formula for the ettringite used in this study is nominally $Ca_6[Al(OH)_6]_2(SO_4)_3 \cdot 25.5H_2O$ with a corresponding formula weight of 1309.3 g/mole. The symmetry is that of the $P31c$ space group with lattice parameters at 10 K of $a = 1.116681(82)$ nm and $c = 2.135366(22)$ nm. The ettringite crystalline structure projected along the c-axis is shown in Fig. 2 with O–H covalent bonds in the water and hydroxyl molecules shown in blue and the longer hydrogen bonds shown in green. Additionally, coordination polyhedra have been shown for calcium, aluminum, and sulfur to aid in visualizing the structural building blocks. It should be noted that those bonds or coordination polyhedra that lie on the edge of the unit cell are incomplete and hence are omitted in the figure. The ettringite crystal structure is observed to consist of calcium and aluminum coordination polyhedra connected in an alternating fashion to form a column. Exterior to the column of calcium and aluminum coordination polyhedra are columns composed of sulfate tetrahedra and channel waters. Fig. 3 provides an illustration of the ettringite structure as viewed down the c-axis of a $2 \times 2 \times 2$ unit cell configuration. Focusing on the central column in Fig. 3, composed of calcium and aluminum coordination polyhedra, the relationship of the exterior columns, consisting

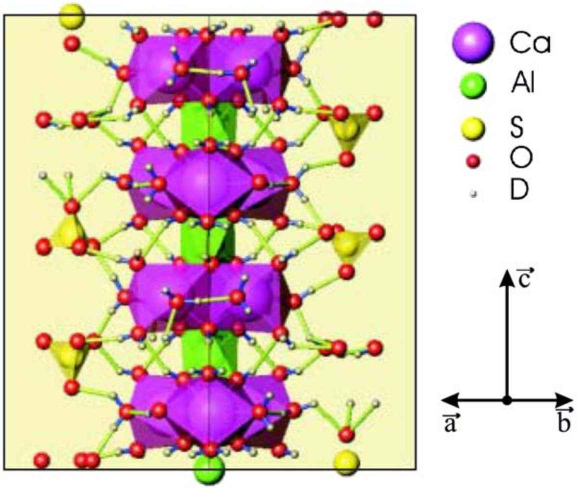

Fig. 2. A projection of the ettringite crystal structure along the *c*-axis, illustrating the hydrogen bonding network. The ettringite unit cell, centered about (0, 0, 0) is displayed with the orientation of the axes as shown below the atom legend.

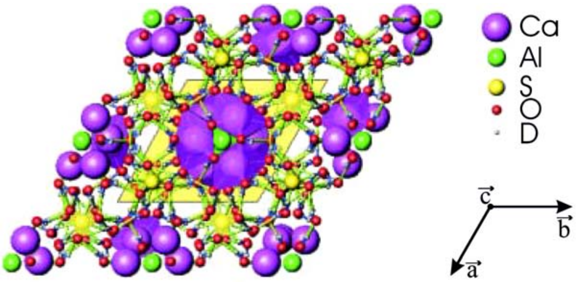

Fig. 3. A 2 × 2 × 2 ettringite unit cell configuration as viewed down the *c*-axis, demonstrating the relationship of the exterior columns to the central column of calcium and aluminum coordination polyhedra. The unit cell, centered about (0, 0, 0) is displayed with the orientation of the axes as shown below the atom legend.

of sulfate tetrahedra and channel waters, to the central column is clearly visible.

3.2. *In situ dehydration*

The initial positions for all atoms were taken to be those of the recent work by Hartman and Berliner [4]. After refining the crystal structure model, allowing for changes in the lattice, isotropic atomic displacement, and scale parameters, the agreement of the data to the model of Hartman and Berliner is quite good as displayed in Fig. 4. The refined lattice parameters for the ettringite sample at 40 °C are $a = 1.123086(10)$ nm and $c = 2.145084(25)$ nm, in close agreement with the non-dehydrated values of Shimada and Young [9].

Fig. 5 summarizes the 40 1-h dehydration data sets. The shading indicates the relative intensity of the diffraction data as a function of time and *d*-spacing. In the figure, the three different panels, from top to bottom, correspond to the dehydration as observed by the +44°, +90°, and +145° SEPD detector banks, respectively. The intensity of any given peak is observed to decrease as a function of time with the final pattern showing very few distinct features. The other remarkable feature is the general decrease in intensity with increasing time at low *d*-spacing, to the left of the (216) reflection, which corresponds to the loss of incoherent scattering from the sample throughout the dehydration process. As noted earlier, deuterium was used in lieu of hydrogen to reduce the large incoherent scattering cross-section of hydrogen. Yet, deuterium has a non-zero incoherent scattering cross-section and hence gives some incoherent background signal as a result of its presence in both the water and hydroxyl molecules of ettringite. Loss of the background signal as a function of time provides further evidence of the removal of water and hydroxyl molecules from the structure. Also of note, there is no splitting or merging of diffraction lines that would signal a phase transformation. The lack of a phase transformation indicates that the overall symmetry of the ettringite unit cell remains unchanged as a result of the dehydration process, contrary to the observations of Bannister et al. [5].

Fig. 6 shows the orientation of oxygen sites within the aluminum and calcium coordination polyhedra for one formula unit of ettringite. In Fig. 6(a), the designators *A*, *B*, and *O* are those due to the model of Skoblinskaya and Krasilnikov [6,7] where *A* and *B* are separate sites for water bonding and the *O* sites represent hydroxyls. The fourth water site suggested by Skoblinskaya and Krasilnikov, the channel waters, are those that lie in the columns exterior to the column of aluminum and calcium coordination polyhedra. The channel water sites are not explicitly shown in either Fig. 6(a) or (b). Fig. 6(b) shows the same configuration as Fig. 6(a) but with the oxygen sites explicitly labeled using the labeling convention of Hartman and Berliner [4]. The dehydration suggested by Skoblinskaya and Krasilnikov [6,7] postulates that the channel water sites, which are bonded only through hydrogen bonds to the central column, are depopulated first. Following the loss of the channel water sites, those water molecules with oxygen atoms located on the *A* sites are removed since the *A* sites have a longer Ca–O bond distance than do those of the *B* sites. After the loss of the channel waters and *A* site waters, the *B* site waters are lost next with the *O* site hydroxyls being the last to be removed in the dehydration process. The investigation by Shimada and Young [9] corroborated the initial stages of the dehydration process of Skoblinskaya and Krasilnikov with the channel waters being removed, followed immediately by the waters at the *A* sites, and then the waters at the *B* sites down to a total loss of 20 waters, or about 29 wt%. However, Shimada and Young concluded, based upon ^{27}Al NMR data, that additional dehydration beyond the loss of 20 waters involved the removal of the *B* site waters and the *O* site hydroxyls simultaneously.

To investigate the dehydration model of Skoblinskaya and Krasilnikov and the observations of Shimada and Young, the in situ dehydration data were grouped into ten

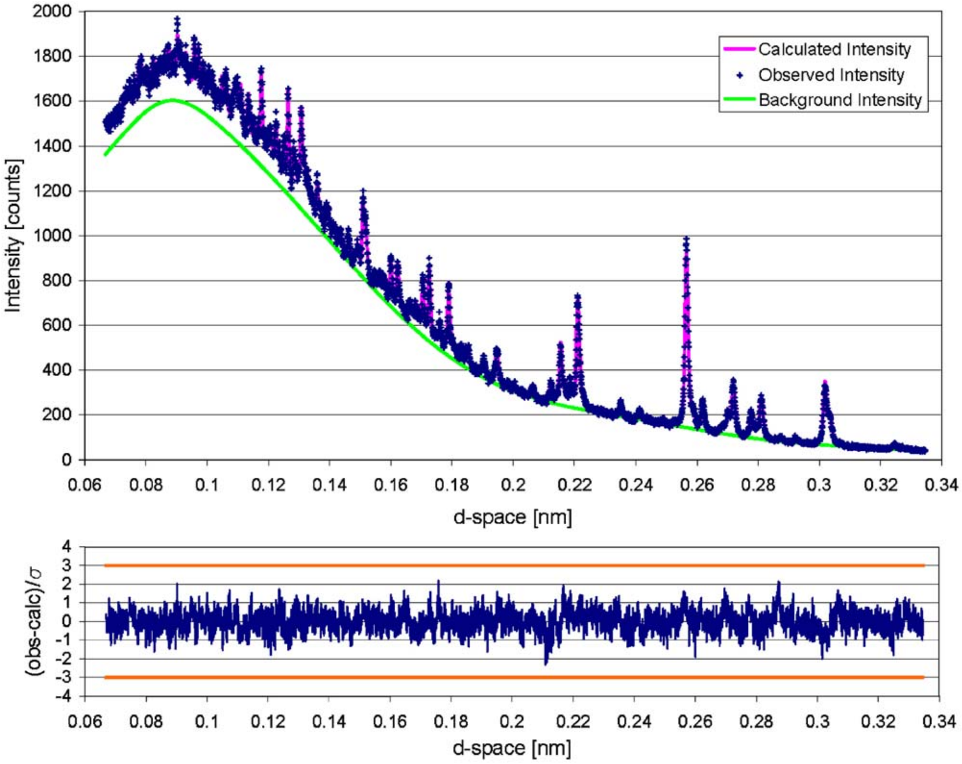

Fig. 4. Fit of the ettringite structural model of Hartman and Berliner to the +145° detector data for the ettringite sample at 40 °C prior to the in situ dehydration (above). The error in the structural model is shown with solid orange lines drawn at $\pm 3\sigma$ (below).

4-h data sets to arrive at data of sufficient statistical quality for structural refinement. Each of the 4-h data sets was then subjected to a structural refinement. Within the refinement, the occupations of oxygen and deuterium atoms associated with a given water or hydroxyl molecule were varied as a molecular unit with the occupation of the various sites, *A*, *B*, *O*, and channel water, allowed to vary independently of one another. Fig. 7 shows the calculated weight loss for the ten 4-h data sets, calculated based on the results of the structural refinements, along with the known initial and final weight losses, as determined from direct measurement of the sample mass, connected by a dashed line. The data points for the weight losses calculated from the structural refinement are given at the median time of each data set. The weight loss for the final data set, 33.62 ± 0.05 wt%, is in reasonable agreement with the final weight loss based upon the actual sample mass of 30.52 ± 0.02 wt%.

Changes in the occupation of the various sites, as labeled in Fig. 6(a), are shown in Fig. 8. Of particular note in the figure is the simultaneous depopulation of all sites, in marked contrast to the dehydration process proposed by Skoblinskaya and Krasilnikov [6,7].

3.3. *Static dehydration measurements by neutron diffraction*

A plausible explanation for the observed differences in the dehydration pathway is that the in situ sample suffered from stratification of the sample, resulting in a mixed dehydration state within the sample. To investigate whether or not stratification of the sample resulted in the observed trends, ettringite samples dehydrated by heat treatment to a known weight loss were investigated in a static measurement.

Data for ettringite samples with 6.16%, 15.6%, 20.5%, and 27.1% weight loss were individually collected on the SEPD instrument at the IPNS at 10 K. The occupations of the oxygen and deuterium atoms associated with a given water molecule were varied as a molecular unit. In addition, the occupation fractions of water molecules were allowed to vary independently of one another instead of grouping them into *A*, *B*, and channel water sites as was done with the in situ data. The oxygen and deuterium occupations associated with a given hydroxyl molecule were allowed to vary independently of one another, with the occupation fraction of each hydroxyl treated separately rather than grouping all the hydroxyls into *O* sites. The hydroxyls were not treated as molecular units because loss of an OH^- results in a local charge imbalance, and it is postulated that this is compensated for by the loss of an H^+ ion from a nearby hydroxyl, resulting in the net loss of an electrically neutral water molecule. The more detailed treatment of the static dehydration data was permitted by the much improved statistical quality of each static dehydration data set, compared to the individual in situ data sets. Fig. 9 demonstrates the quality of the fit of the structural model to the +145° SEPD detector data for the material dehydrated to a weight loss of 6.16% and 27.1%. Similar to the in situ dehydration, a decrease in the relative diffraction peak intensity for any given reflection is observed with increasing levels of dehydration. Additionally, the widths of the diffraction peaks are also observed to increase with increasing levels of dehydration. Table 1 gives the site occupancy for the various atomic sites for each of the static dehydration data sets as well as the site occupancies for the unaltered material [4]. Fig. 10 shows the calculated weight loss based upon the site occupancies of Table 1 on the vertical axis with the weight loss based upon actual sample weights on the horizontal axis. The straight line in the figure corresponds to equal calculated and measured weight losses and is drawn as a visual aid and not as a fit to the data. The largest discrepancies exist for the specimens with measured weight losses of 6.16 and 27.1 wt%, for which the calculated weight losses are 9.2±0.3 and 24.6±0.4 wt%, respectively. Overall, the agreement between the calculated and measured weight losses is good. Fig. 11 shows the individual water and hydroxyl sites grouped into the site notation of Skoblinskaya and Krasilnikov [6,7] for comparison with the in situ changes shown in Fig. 8. The static dehydration data, shown in Fig. 11, exhibit features very similar to the in situ data. The *A* and *B* site waters are observed to depopulate at a nearly equal rate, with the hydroxyl *O* sites simultaneously depopulating slightly slower. The simultaneous loss of the hydroxyl molecules is consistent with the ^{27}Al NMR results of Shimada and Young [9] where changes in the NMR signal were evident throughout the dehydration process. However, Shimada and Young only associated the changes in the NMR signal with loss of hydroxyls from the ettringite structure later in the dehydration process when the changes in the NMR signal had become more pronounced. The channel water occupancy decreases with the exception of the final data point, which exhibits a slight increase. The slight increase in the channel water occupation may be a dynamic effect whereby the channel water sites act as a conduit for water diffusion amongst the calcium coordination polyhedra in the severely dehydrated material. The lattice parameter changes for the static dehydration samples, shown in Fig. 12, exhibit features

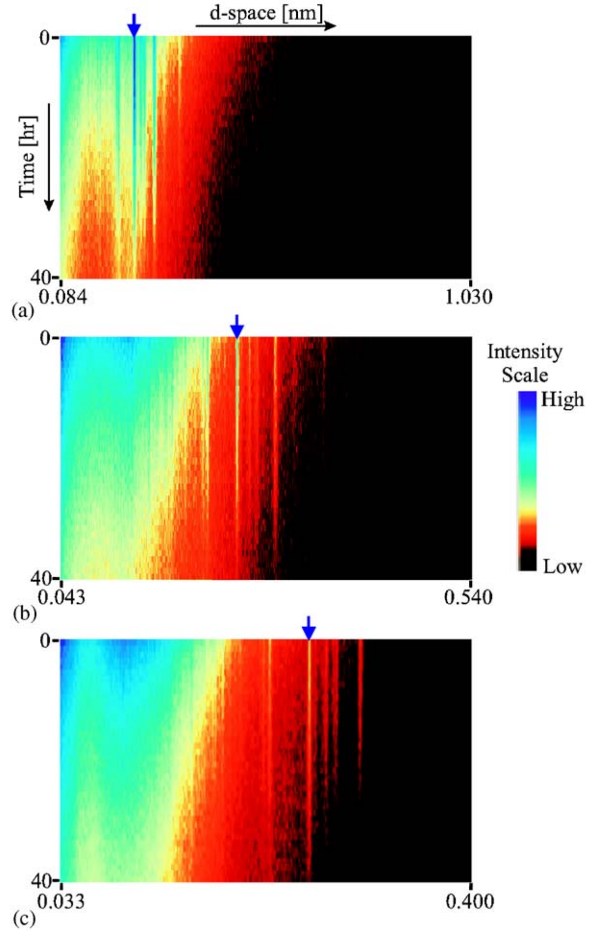

Fig. 5. Time evolution of the diffraction patterns for the in situ dehydration of ettringite as viewed by the (a) +44°, (b) +90°, and (c) +145° detector banks of the SEPD instrument. The horizontal axis represents *d*-spacing and increases from left to right. The vertical axis represents time, increasing from top to bottom over the 40 h duration of the dehydration. The arrow at the top of each panel corresponds to the ettringite (216) reflection.

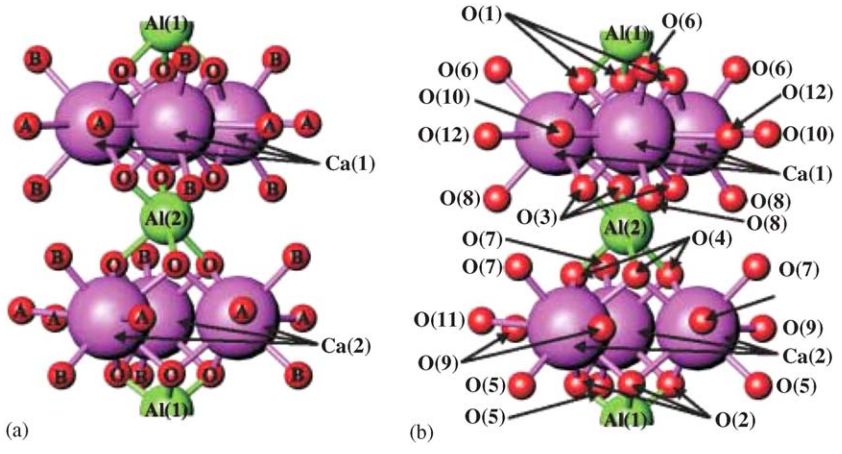

Fig. 6. Orientation of oxygen sites on the column of aluminum and calcium coordination polyhedra in the notation of (a) Skoblinskaya and Krasilnikov and (b) Hartman and Berliner.

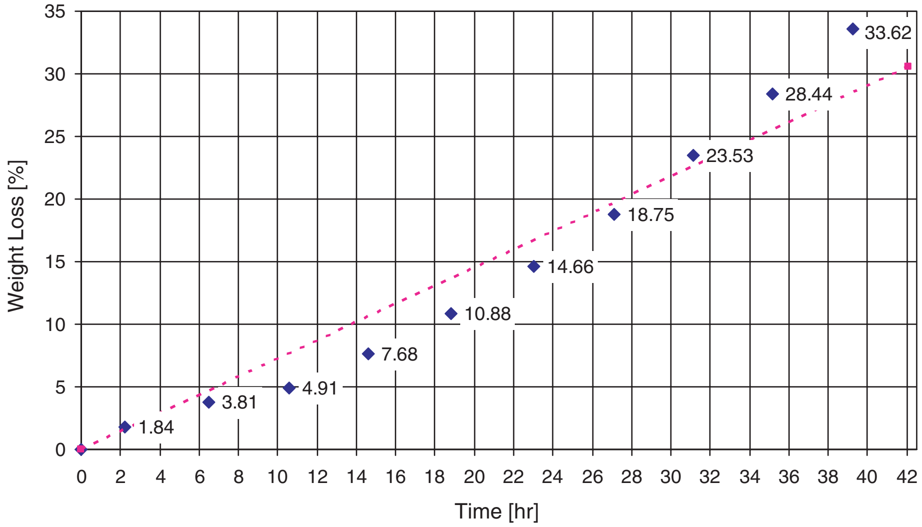

Fig. 7. Calculated weight losses from neutron structural refinements for the in situ dehydration of ettringite at 50 °C (diamonds) with the directly measured weight losses at the beginning and end of the measurement (squares), connected by the dashed line. Estimated standard deviations for the data points, based upon the structural refinements, are 0.05 wt%.

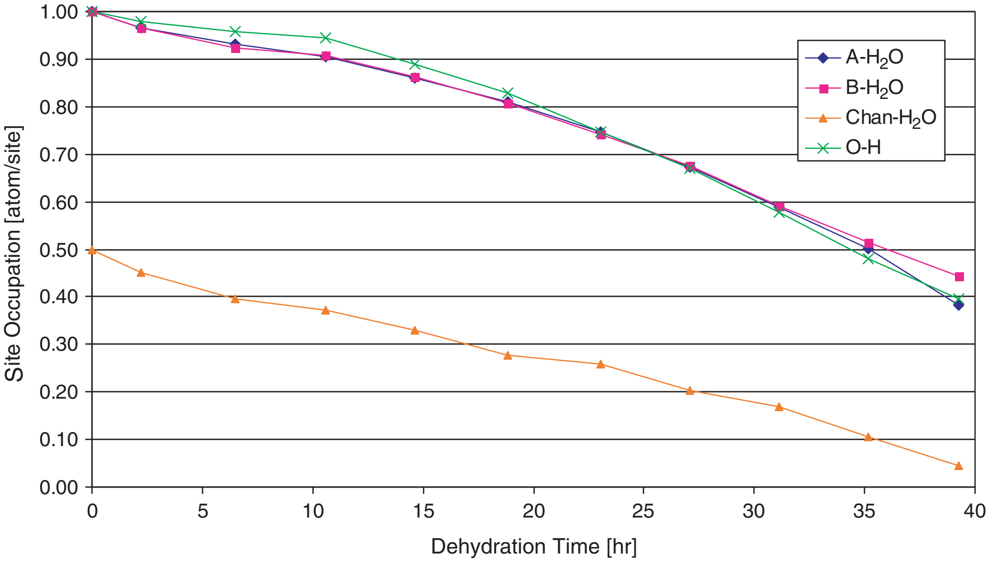

Fig. 8. Variation in the occupation of atomic sites based upon the results of the structural refinement for the in situ dehydration of ettringite at 50 °C.

similar to those of the X-ray work of Shimada and Young [9] with an expansion along the *a*-axis and a contraction along the *c*-axis with increasing dehydration. The numerical values of the lattice parameters in the present work are smaller than those of Shimada and Young as a result of data collection at 10 K to minimize atomic thermal motions. For direct comparison to the work of Shimada and Young, the weight loss axis of any graph in the present work may be converted to equivalent water molecules remaining in the structure by dividing the scale by −1.527 wt%/water unit and adding 31.5.

Table 2 lists the mean coordination of the aluminum and calcium atoms for the static dehydration measurements based upon the results of the structural refinement. The mean coordination numbers vary slightly from those of previous researchers as a result of incorporating a greater loss of hydroxyl molecules and also maintaining some level of channel water occupation. The net result is that the ettringite crystal structure maintains long-range order with the mean calcium coordination reduced to a value of ~4.5 and the mean aluminum coordination decreased to a value of ~3.6, based on the arithmetic average of Ca(1) and Ca(2) for the calcium coordination and Al(1) and Al(2) for the aluminum coordination.

3.4. Static dehydration measurements by ^1H NMR spectroscopy

We studied three ettringite samples by NMR: A fully hydrated sample, one dehydrated to 6.98% weight loss,

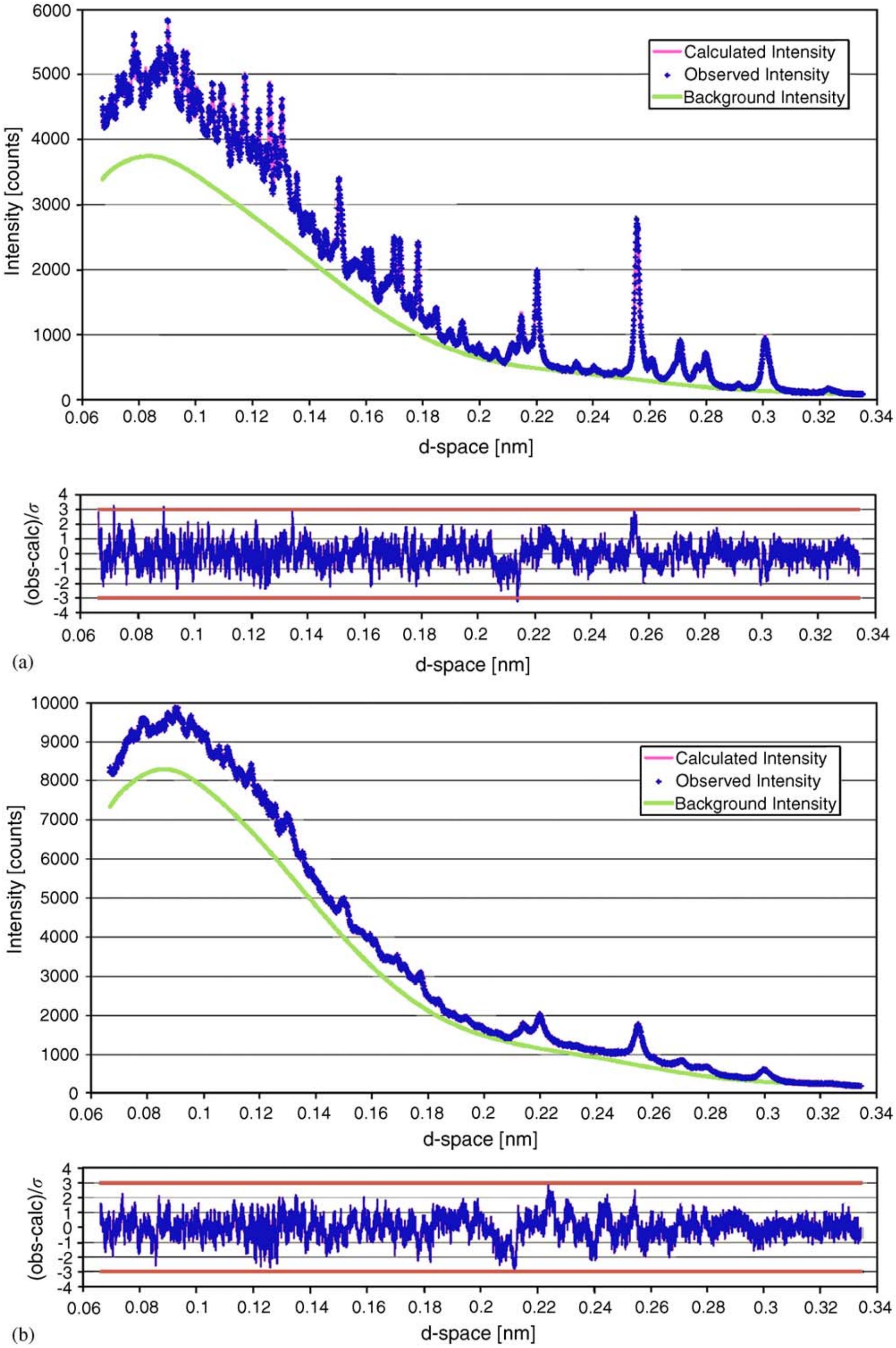

Fig. 9. Fit of the structural model to the static dehydration samples with (a) 6.16%, (b) 27.1% weight loss.

and one dehydrated to 19.9% weight loss. All three samples were in the NMR rigid-lattice limit at and below 130 K, as demonstrated in Fig. 13 for the fully hydrated sample. At 296 K there is significant motional narrowing of the proton spectrum, but at 120 K motions on the NMR timescale (tens of microseconds) have been frozen out, broadening the spectrum to its rigid-lattice width. Evidently the rigid-lattice limit has been reached at 120 K because no further spectral broadening is observed even 43 K colder, at 77 K. Note that in Fig. 13, the 120 K spectrum was measured at a frequency of 85.04 MHz, and the 77 K spectrum at 39.99 MHz, with negligible difference. Indeed, the lineshape and width are expected to be independent of frequency because dipole interactions are dominant. The largest chemical shifts one could reasonably expect in proton NMR, 10 ppm (850 Hz at 85.04 MHz), are

Table 1
Site occupancies (atom/site) for the static dehydration samples based upon Rietveld structural refinement with estimated standard deviations given in parentheses

Site label	Calculated weight loss (%)				
	0.00	9.2(3)	14.5(3)	19.0(3)	24.6(4)
O(1)	1.0000	0.899(10)	0.893(12)	0.882(11)	0.828(11)
D(1)	0.9623(30)[a]	0.829(10)	0.669(11)	0.455(12)	0.053(14)
O(2)	1.0000	0.821(10)	0.746(12)	0.653(12)	0.287(13)
D(2)	0.9623(30)[a]	0.712(9)	0.748(10)	0.776(9)	0.487(11)
O(3)	1.0000	0.842(11)	0.850(13)	0.806(13)	0.845(13)
D(3)	0.9623(30)[a]	0.942(10)	0.792(11)	0.564(11)	0.736(10)
O(4)	1.0000	0.967(11)	0.768(13)	0.655(12)	0.578(13)
D(4)	0.9623(30)[a]	0.820(9)	0.651(10)	0.573(10)	0.733(9)
O(5)	1.0000	0.778(5)	0.705(5)	0.653(5)	0.519(5)
D(5a)	0.9623(30)[a]	0.748(4)	0.679(5)	0.628(5)	0.500(5)
D(5b)	0.9623(30)[a]	0.748(4)	0.679(5)	0.628(5)	0.500(5)
O(6)	1.0000	0.885(4)	0.819(5)	0.777(5)	0.490(6)
D(6a)	0.9623(30)[a]	0.852(4)	0.788(5)	0.747(5)	0.472(6)
D(6b)	0.9623(30)[a]	0.852(4)	0.788(5)	0.747(5)	0.472(6)
O(7)	1.0000	0.864(5)	0.790(5)	0.684(5)	0.621(5)
D(7a)	0.9623(30)[a]	0.831(5)	0.760(5)	0.658(5)	0.597(5)
D(7b)	0.9623(30)[a]	0.831(5)	0.760(5)	0.658(5)	0.597(5)
O(8)	1.0000	0.863(5)	0.684(6)	0.574(5)	0.544(6)
D(8a)	0.9623(30)[a]	0.830(5)	0.658(5)	0.553(5)	0.524(6)
D(8b)	0.9623(30)[a]	0.830(5)	0.658(5)	0.553(5)	0.524(6)
O(9)	1.0000	0.810(5)	0.723(5)	0.663(5)	0.555(5)
D(9a)	0.9623(30)[a]	0.780(4)	0.695(5)	0.638(5)	0.534(5)
D(9b)	0.9623(30)[a]	0.780(4)	0.695(5)	0.638(5)	0.534(5)
O(10)	1.0000	0.747(4)	0.685(5)	0.584(5)	0.437(6)
D(10a)	0.9623(30)[a]	0.719(4)	0.659(5)	0.562(5)	0.420(6)
D(10b)	0.9623(30)[a]	0.719(4)	0.659(5)	0.562(5)	0.420(6)
O(11)	1.0000	0.825(5)	0.658(5)	0.563(5)	0.478(6)
D(11a)	0.9623(30)[a]	0.794(5)	0.633(5)	0.542(5)	0.460(6)
D(11b)	0.9623(30)[a]	0.794(5)	0.633(5)	0.542(5)	0.460(6)
O(12)	1.0000	0.851(5)	0.759(5)	0.642(6)	0.544(6)
D(12a)	0.9623(30)[a]	0.819(4)	0.730(5)	0.618(5)	0.523(6)
D(12b)	0.9623(30)[a]	0.819(4)	0.730(5)	0.618(5)	0.523(6)
O(19)	0.4986(70)	0.312(6)	0.221(7)	0.174(7)	0.304(8)
D(19a)	0.4774(70)[a]	0.300(6)	0.212(6)	0.168(7)	0.293(7)
D(19b)	0.4774(70)[a]	0.300(6)	0.212(6)	0.168(7)	0.293(7)

[a] The initial ratio of deuterium to oxygen of 0.9623 in the hydroxyl and water molecules takes into account imperfect deuteration of the sample. The ratio is maintained for the water molecules, but it is allowed to vary for the hydroxyl molecules to account for electronic charge balance.

insignificant on the scale of these linewidths. We also obtained spectra at 296 K at both frequencies and they overlayed well.

The spectra used in our analyses were obtained using the technique of magic echoes [16–18]. Solids with broad spectra, such as the present ettringite samples, have free induction decays (FIDs), which are short in time. It is not possible to record the very-early time portion of a FID following an RF pulse since the FID starts while the pulse is still on, and the NMR resonant circuit and the receiver need time to recover after the pulse has ended. Missing the first few microseconds of a FID which itself persists for only about 20 μs can significantly affect the resulting spectrum. Use of a short excitation pulse and "patching" the early time portion of the FID with a fitted Gaussian curve often does well at recovering the true lineshape, but still involves a certain amount of subjectivity. In like-spin, dipolar-coupled systems, the magic echo technique refocuses all of the spin interactions at a time well beyond that needed for receiver recovery into an echo that nearly perfectly models the FID. This echo is not missing any early time data, and so can be directly Fourier transformed into an accurate frequency spectrum. We used the pulse sequence $\tau_x - \tau_{\bar{x}} - 90^\circ_y$ to form magic echoes. This is like the pulse sequence used in Ref. [18], except that our time-reversal pulse is broken into two pulses of equal duration and opposite phase, τ_x and $\tau_{\bar{x}}$, which eliminates dephasing of the echo due to inhomogeneous RF field.

Ettringite is a system well suited to the magic echo technique. The only spin interaction in ettringite not refocused by the magic echo is the unlike-spin, dipole interaction between ^{27}Al nuclei and nearby protons. This interaction turns out to be a very small contributor to spectral linewidth, as we verified experimentally and

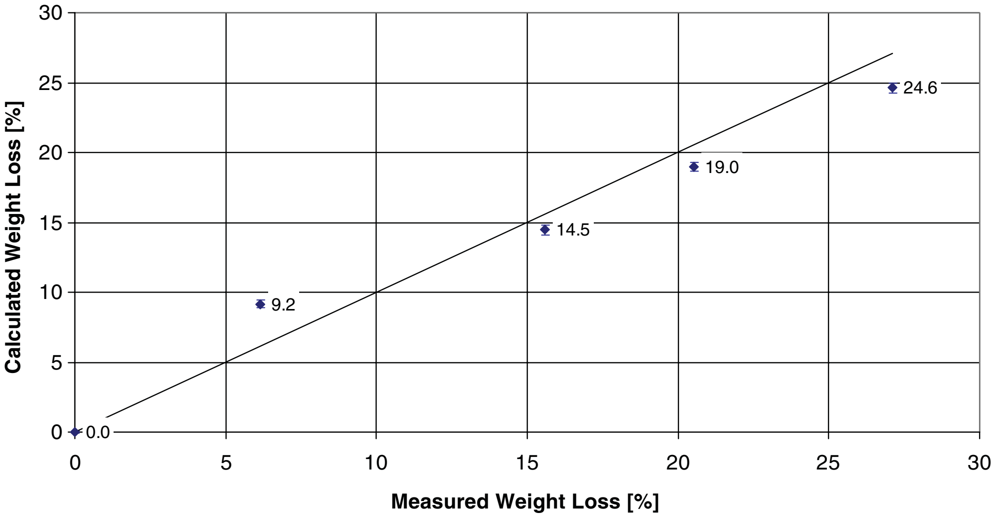

Fig. 10. Comparison of calculated versus measured weight losses for the thermally treated ettringite specimens. Numerical values for calculated weight losses are shown with error bars at $\pm 3\sigma$. The straight line corresponds to equal calculated and measured weight losses and is drawn as a visual aid and not as a fit to the data.

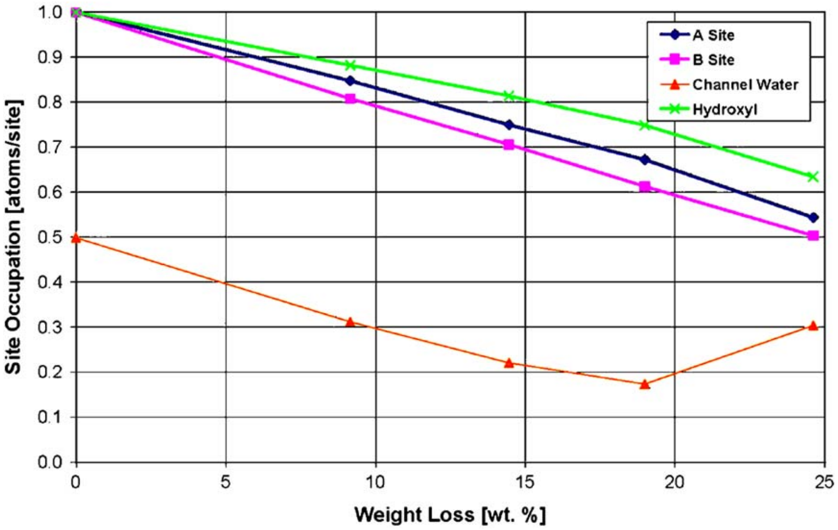

Fig. 11. Variation of atomic site occupancies in the notation of Skoblinskaya and Krasilnikov for the static dehydration samples.

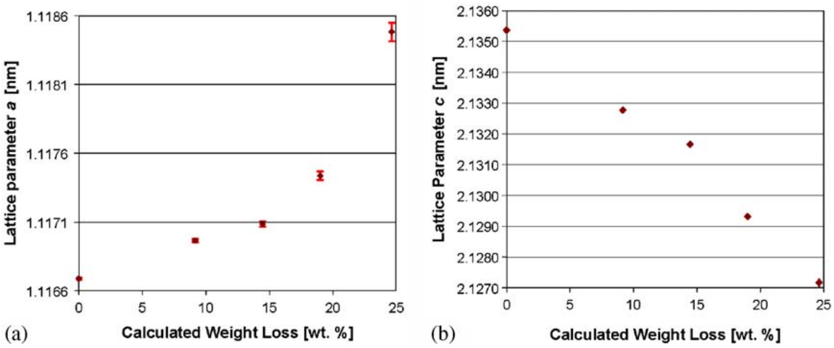

Fig. 12. Variation of ettringite lattice parameters for static dehydration samples at 10 K. Error bars are shown at $\pm 1\sigma$.

theoretically. Fig. 14 shows rigid-lattice spectra obtained two ways for fully hydrated ettringite. One curve is the Fourier transform of a FID following a short (500 ns) excitation pulse, obtained at 120 K and 85.04 MHz. Before transforming, the first 4.6 μs in the time-domain were replaced with a Gaussian curve fitted to the early time

Table 2
Mean coordination numbers of the calcium and aluminum atoms for the static dehydration samples with estimated standard deviations given in parentheses

Atom	Calculated weight loss (%)				
	0.00	9.2(3)	14.5(3)	19.0(3)	24.6(4)
Ca(1)	8.00	6.83(2)	6.43(3)	5.95(3)	5.36(3)
Ca(2)	8.00	6.85(2)	5.90(3)	5.18(3)	3.90(3)
Al(1)	6.00	5.16(4)	4.92(5)	4.61(5)	3.35(5)
Al(2)	6.00	5.43(5)	4.85(6)	4.38(5)	4.27(6)
All Ca sites	8.00	6.84(2)	6.17(2)	5.57(2)	4.63(2)
All Al sites	6.00	5.29(3)	4.89(3)	4.49(4)	3.81(4)

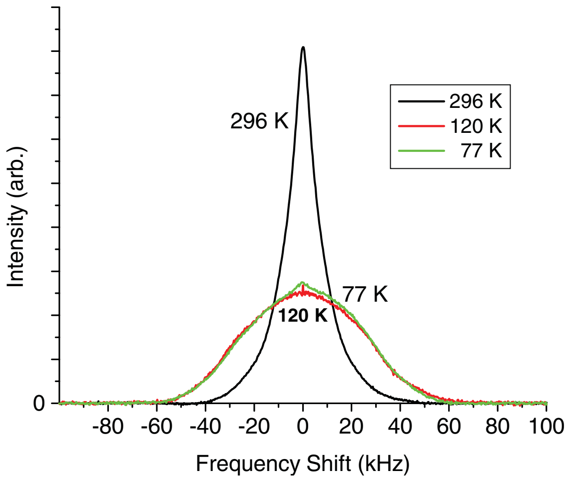

Fig. 13. Proton NMR spectra of fully-hydrated ettringite. The 296 and 120 K spectra were taken at 85.04 MHz, the 77 K spectrum at 39.99 MHz. The spectral areas are normalized. The ettringite is evidently already in the NMR rigid lattice limit at 120 K. The lineshape is independent of the measurement frequency at low temperatures, as expected when dipolar interactions dominate.

portion of the FID. The other spectrum in Fig. 14 is the Fourier transform of a magic echo obtained at 77 K and 39.99 MHz. Each time reversal pulse τ was 14.08 μs in duration for a total duration of 28.16 μs. The spectra overlay well, indicating that the magic echo is refocusing all of the significant spin interactions. We also calculated the effect of the ^{27}Al–^{1}H dipole interaction in all of our theoretical spectra. Even for the 19.9% weight loss sample in which the unlike-spin interaction contributed most (relatively) to spectral linewidth, neglecting this interaction reduced the FWHM by only 2.0% for our model of dehydration, and 4.4% for the model proposed by Shimada and Young. So from both experimental and theoretical standpoints, it is clear that the magic echo technique will work well to find accurate frequency spectra for ettringite.

With the atomic positions from the structural refinements from the static dehydration neutron diffraction measurements (Section 3.3), we were able to construct theoretical NMR frequency spectra for the hydrogen site occupancies given by both our model of dehydration and that proposed by Shimada and Young. Recall that the neutron diffraction work used deuterated ettringite while the NMR work used hydrogenated ettringite. Since H_2O and D_2O have different weights, weight loss percentages in deuterated ettringite are not directly comparable with those in hydrogenated ettringite. Nevertheless, comparisons can be made by recognizing that 1 H_2O molecule represents 1.4348% of the formula weight of hydrogenated ettringite, and 1 D_2O molecule represents 1.5168% of the formula weight of deuterated ettringite. Based on these numbers the 6.16% weight loss deuterated ettringite sample is equivalent to a 5.83% weight loss hydrogenated sample, and the 20.5% weight loss deuterated sample is equivalent to a 19.4% weight loss hydrogenated sample. We used the atomic positions found by neutron diffraction of the 6.16% weight loss (deuterated) sample for calculating the theoretical NMR spectra of the 6.98% weight loss (hydrogenated) sample, and atomic positions of the 20.5% weight loss (deuterated) sample for calculating the theoretical NMR spectra of the 19.9% weight loss (hydrogenated) sample.

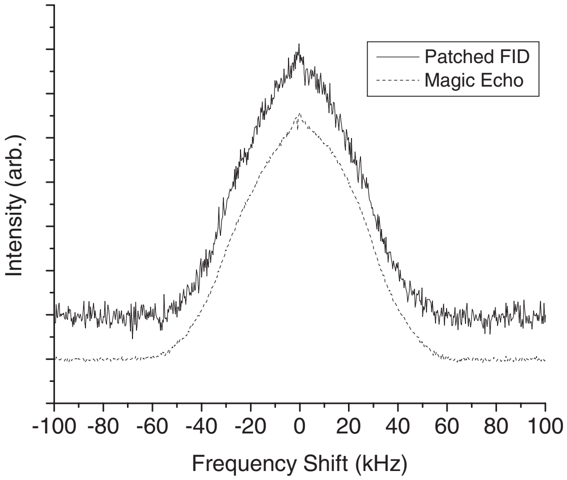

Fig. 14. Rigid-lattice spectra with normalized areas from a Gaussian-patched FID (120 K, 85.04 MHz) and a magic echo (77 K, 39.99 MHz) for fully-hydrated ettringite. The two spectra are shifted vertically for clarity.

A quantity which we will refer to often is the "second moment", M_2, which originated with Van Vleck's method of moments [15,19]. The second moment of a resonance curve is its mean-squared linewidth, and is proportional to the squared strength of the dipolar field at the site of the nucleus responsible for the spectrum, as well as that nucleus' squared gyromagnetic ratio. In calculating a second moment, contributions from all of the nearby dipolar nuclei are added together. Since magnetic dipole interactions drop off with the cube of internuclear spacings, contributions to M_2 drop off with the sixth power of internuclear spacings. So for a nucleus at a particular crystalline site, the sphere of neighbors adding appreciably to its M_2 is of a small radius—about 12 Å in our system.

Ettringite has four crystallographically distinct hydroxyl proton sites (*O* sites in the notation of Skoblinskaya and Krasilnikov) and nine distinct water sites (*A* sites, *B* sites, and channel waters). The hydroxyl protons do not have any particularly close proton neighbors, so they should contribute a more or less Gaussian lineshape [20] to the overall ettringite spectrum, according to the central limit theorem. Thus, in our theoretical NMR spectra, each hydroxyl site contributed a Gaussian line weighted by that site's occupancy, and of a linewidth determined by the hydroxyl proton's second moment.

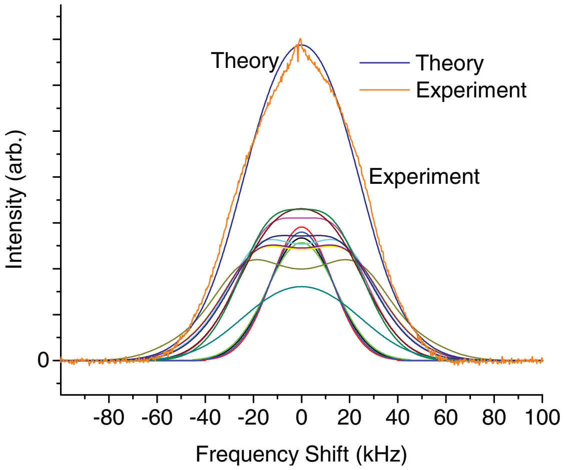

Fig. 15. Calculated NMR spectrum (blue) of fully-hydrated ettringite plotted with the associated rigid-lattice (77 K) experimental spectrum (orange) measured at 39.99 MHz. Also shown are the nine sub-spectra (broad) contributed by crystallographically distinct waters, and the four sub-spectra (narrow) from distinct O–H protons. The area of each sub-spectrum is proportional to its associated site's occupancy. These 13 sub-spectra were added to yield the overall theory spectrum, the area of which was subsequently scaled by 0.2 for ease of viewing on this plot. The area of the experimental spectrum has been normalized to that of the theory spectrum.

On the other hand, a structural water in the ettringite powder should contribute to the overall spectrum an axially symmetric Pake powder pattern convoluted with Gaussian broadening, the width of the broadening curve coming from a second moment calculation (for convenience taken at the midpoint of the water's H–H connector). The classic example of this is water in gypsum ($CaSO_4 \cdot 2H_2O$), studied by Pake [21]. The local magnetic field felt by one proton on a bound water molecule is affected strongly by the field of the molecule's other proton. In a powder, all orientations of the H–H separator relative to the external magnetic field B_0 are equally represented, which gives rise to the powder pattern lineshape, broadened examples of which appear in Fig. 15. The cusp-to-cusp frequency splitting [20,21] of a given water molecule's powder pattern is a sensitive function of that molecule's H–H separation [21]. In our theoretical NMR spectra, each distinct water contributed a broadened powder pattern weighted by that site's occupancy.

The sum of the weighted spectral contributions from hydroxyl and water protons give a spectrum in good agreement with experiment for fully hydrated ettringite, as shown in Fig. 15. The H–H separations of the water protons, reported by neutron diffraction from fully occupied ettringite, have all been scaled by 1.020. While large-amplitude motions on the NMR timescale have been frozen out in our low-temperature experimental spectra, ultrahigh frequency (gigahertz) linear and, more importantly, torsional vibrations remain, which are known [22–25] to cause NMR to report internuclear separations typically longer than those measured by neutron diffraction. For example, Henry and Szabo [22] calculated the effects of such motions on the C–H bond lengths of methylene groups in propane and octane, and reported increases ranging from 1.0% to 6.3%. The present scaling factor improves the fit slightly and was chosen empirically.

Fig. 16 compares our theoretical calculations with experimental results for the 6.98% and 19.9% weight

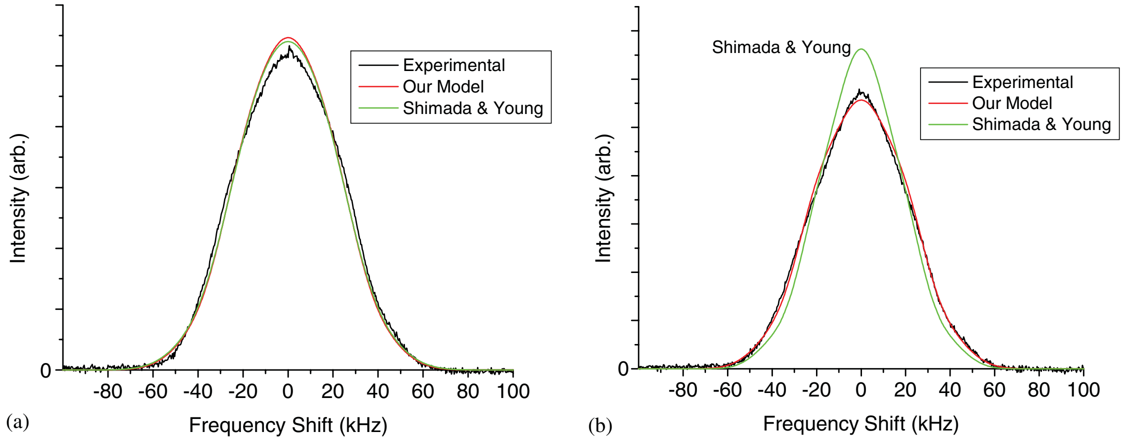

Fig. 16. NMR rigid-lattice spectra (125 K, 85.04 MHz—the curves with obvious noise) plotted with theoretical curves from both our model of dehydration and that of Shimada and Young for 6.98% weight loss ettringite (a) and 19.9% weight loss ettringite (b). The two models are indistinguishable by NMR at 6.98% weight loss, but at 19.9% weight loss our model exhibits a much better fit to the data.

loss, statically dehydrated samples of ettringite. At each level of dehydration, a theoretical spectrum was calculated based on the hydrogen site occupancies predicted by our dehydration model, and that of Shimada and Young. Again, the H–H separations of the water protons, reported by neutron diffraction, were scaled by 1.020.

At the 6.98% weight loss level of dehydration, there is not sufficient difference between the dehydration model predictions to choose one over the other. However, at the 19.9% weight loss level of dehydration, the theoretical spectra argue strongly in favor of our simultaneous site depopulation model of dehydration over Shimada and Young's (and Skoblinskaya and Krasilnikov's) more step-wise depopulation model of dehydration. To account for a 19.9% weight loss, the Shimada and Young model of dehydration calls for removal of all channel waters and *A* site waters, leaving only the *B* site waters to contribute amplitude in the broad parts of the associated NMR spectrum. At the same time, amplitude near the center is overstated due to the predicted full occupancy of the O–H proton sites. On the other hand, the theoretical NMR spectrum based on our hydrogen site occupancies (Table 1) fits the experimental spectrum well.

4. Conclusion

The dehydration pathway of ettringite has been investigated using pulsed neutron TOF diffraction techniques in combination with Rietveld crystal structure refinement. The dehydration process was followed in situ using a specially designed sample holder and with static measurements on samples that were thermally treated in the laboratory. The results from the in situ and static pulsed neutron TOF diffraction investigations are in good agreement with each other and show a simultaneous loss of water and hydroxyl molecules from the ettringite structure, based upon direct measurement of the water and hydroxyl molecule occupancies from structural refinement of neutron diffraction data. The hydrogen NMR rigid-lattice, dipole-broadened spectra support these conclusions. These observations are contrary to prior investigations, which relied upon indirect measurements to infer the occupation and order of removal of the water and hydroxyl molecules. Static measurements of a laboratory dehydrated ettringite sample indicated that the material retained long-range order even after a weight loss of 27.1%, equivalent to the loss of 17.7 water units. In situ dehydration measurements indicated that the threshold for transition to an amorphous state, as seen by neutrons, occurs at a loss of ~30 wt%, corresponding to the loss of 19.6 water units. The dehydration process results in a 0.2% increase in the *a*-axis lattice parameter with a simultaneous 0.4% contraction of the *c*-axis.

Acknowledgments

This work has greatly benefited from the use of the Intense Pulsed Neutron Source (IPNS) at Argonne National Laboratory. IPNS is funded by the US Department of Energy, BES-Materials Science, under contract W-31-109-ENG-38. Funding for this work at the University of Michigan and at Washington University was provided in part by National Science Foundation Grant CMS-0196400. The authors also wish to thank Dr. James Jorgensen and Mrs. Simine Short for their assistance in the conduct of this experiment.

References

[1] H.F.W. Taylor, Cement Chemistry, second ed., Thomas Telford, London, 1997.

[2] M. Santhanam, M.D. Cohen, J. Olek, Sulfate attack research—whither now?, Cement Concrete Res. 31 (2001) 845–851.

[3] H.F.W. Taylor, C. Famy, K.L. Scrivener, Delayed ettringite formation, Cement Concrete Res. 31 (2001) 683–693.

[4] M.R. Hartman, R. Berliner, Reinvestigation of the structure of ettringite by time-of-flight neutron powder diffraction techniques, Cement Concrete Res. 36 (2006) 364–370.

[5] F.A. Bannister, M.H. Hey, J.D. Bernal, Ettringite from Scawt Hill, Co., Antrim, Mineral. Mag. J. Mineral. Soc. 24 (1936) 324–329.

[6] N.N. Skoblinskaya, K.G. Krasilnikov, Changes in crystal structure of ettringite on dehydration 1, Cement Concrete Res. 5 (1975) 381–394.

[7] N.N. Skoblinskaya, K.G. Krasilnikov, L.V. Nikitina, V.P. Varlamov, Changes in crystal structure of ettringite on dehydration 2, Cement Concrete Res. 5 (1975) 419–432.

[8] A.E. Moore, H.F.W. Taylor, Crystal Structure of Ettringite, Acta Crystallogr. B 26 (1970) 386–393.

[9] Y. Shimada, J.F. Young, Structural changes during thermal dehydration of ettringite, Adv. Cement Res. 13 (2001) 77–81.

[10] J.D. Jorgensen, J. Faber, J.M. Carpenter, R.K. Crawford, J.R. Haumann, R.L. Hitterman, R. Kleb, G.E. Ostrowski, F.J. Rotella, T.G. Worlton, Electronically focused time-of-flight powder diffractometers at the intense pulsed neutron source, J. Appl. Crystallogr. 22 (1989) 321–333.

[11] H.M. Rietveld, A profile refinement method for nuclear and magnetic structures, J. Appl. Crystallogr. 2 (1969) 65–71.

[12] A.C. Larson, R. B. Von Dreele, General Structure Analysis System (GSAS), Los Alamos National Laboratory Report LAUR 86–748, 2000.

[13] B.H. Toby, EXPGUI, a graphical user interface for GSAS, J. Appl. Crystallogr. 34 (2001) 210–213.

[14] R.A. Young (Ed.), The Rietveld Method, Oxford University Press, Oxford, 1993.

[15] C.P. Slichter, Principles of Magnetic Resonance, Springer, New York, 1996.

[16] W.-K. Rhim, A. Pines, J.S. Waugh, Time-reversal experiments in dipolar-coupled spin systems, Phys. Rev. B 3 (3) (1971) 684–696.

[17] W.-K. Rhim, H. Kessemeier, Transverse-magnetization recovery in the rotating frame, Phys. Rev. B 3 (11) (1971) 3655–3661.

[18] R.C. Bowman Jr., W.-K. Rhim, A simple magic-echo sequence for second-moment measurements, J. Magn. Reson. 49 (1982) 93–98.

[19] J.H. Van Vleck, The dipolar broadening of magnetic resonance lines in crystals, Phys. Rev. 74 (1948) 1168–1183.

[20] A. Abragam, The Principles of Nuclear Magnetism, Clarendon Press, Oxford, 1961.

[21] G.E. Pake, Nuclear resonance absorption in hydrated crystals: fine structure of the proton line, J. Chem. Phys. 16 (1948) 327–336.

[22] E.R. Henry, A. Szabo, Solid state line shapes and NMR relaxation, J. Chem. Phys. 82 (11) (1985) 4753–4761.

[23] J. Schaefer, R.A. McKay, E.O. Stejskal, W.T. Dixon, Dipolar rotational spin-echo ^{13}C NMR of polymers, J. Magn. Reson. 52 (1983) 123–129.

[24] G. Lipari, A. Szabo, Model-free approach to the interpretation of nuclear magnetic resonance relaxation in macromolecules. 1. Theory and range of validity, J. Am. Chem. Soc. 104 (1982) 4546–4559.

[25] G. Lipari, A. Szabo, Model-free approach to the interpretation of nuclear magnetic resonance relaxation in macromolecules. 2. Analysis of experimental results, J. Am. Chem. Soc. 104 (1982) 4559–4570.